

Article

Experimental and Geant4 Simulation Study of MURA Mask for Scintimammography

Mohammed A. Alnafea ¹, Khaled Shamma ² and Omrane Kadri ^{1,3,*}

¹ Department of Radiological Sciences, College of Applied Medical Sciences, King Saud University, P.O. Box 10219, Riyadh 11433, Saudi Arabia;alnafea@ksu.edu.sa

² Department of Physics and Astronomy, College of Science, King Saud University, Riyadh 11451, Saudi Arabia; 436107395@student.ksu.edu.sa

³ National Center for Nuclear Sciences and Technologies, Tunis 2020, Tunisia

* Correspondence: okadri@cern.ch

Abstract: Gamma rays have been extensively investigated for breast imaging using collimators; however, the coded-aperture technique needs to be investigated more. In this paper, we propose an experimental study and Geant4 simulations of MURA mask breast imaging. First, we compare the experimental data against the simulation results carried out using Geant4 (version 10.4) and accreditation phantom. Second, we virtually extend our work by changing the tumor-to-background (TBR) and lesion location parameters. We used ^{99m}Tc as a radioactive source. Good agreement has been seen for the benchmark stage, especially in terms of tumor localization. Moreover, the calculated full width at half maximum (FWHM) and contrast for decoded images (having average values of 8 and 3.5 for TBR between 2 and 10) permitted us to conclude that we can accurately localize small lesions up to lower TBR values by following the decoding procedure of deducing the image of a “blank phantom” (phantom with TBR = 1) every time within a matlab-based program. Hence, this work can be considered a continuously added value to previous investigations for scintimammography imaging.



Citation: Alnafea, M.A.; Shamma, K.; Kadri, O. Experimental and Geant4 Simulation Study of MURA Mask for Scintimammography. *Appl. Sci.* **2022**, *12*, 4890. <https://doi.org/10.3390/app12104890>

Academic Editor: Miguel Alcaraz

Received: 27 March 2022

Accepted: 4 May 2022

Published: 12 May 2022

Publisher's Note: MDPI stays neutral with regard to jurisdictional claims in published maps and institutional affiliations.



Copyright: © 2022 by the authors. Licensee MDPI, Basel, Switzerland. This article is an open access article distributed under the terms and conditions of the Creative Commons Attribution (CC BY) license (<https://creativecommons.org/licenses/by/4.0/>).

Keywords: MURA mask; Geant4; scintimammography; FWHM; contrast

1. Introduction

The detection, localization and mapping of radiation-emitting sources are crucial in nuclear decommissioning, decontamination and maintenance procedures [1–3], especially for nuclear medicine imaging. Among the existing medical imaging modalities, we can cite scintimammography, which uses radioactive substance (radiopharmaceutical) and a special camera for breast imaging, as breast cancer tissues attract more radioactive material than healthy tissues [4]. The reason for this is that cancer cells grow and divide more rapidly. Such rapid growth causes the radioactive isotope to accumulate in larger amounts in tumors. Moreover, through the use of coded-aperture gamma-ray imaging systems, a radioactive distribution map can be superimposed on an optical image as a reference for the localization of radioactive hot-spots [5]. It has been extensively developed to improve its capabilities in terms of lightness, usability, sensitivity, spectral capability, etc. [6–10]. Within that context, the modified uniformly redundant array (MURA) mask has been widely used, for which a specific aperture pattern of holes (an open area) represents half of the collimator area and allows us to minimize exposure to that half [11]. The majority of systems are currently designed to produce images under far-field conditions, where images appear nearly perfect. As a result, the distances between imaging systems and radioactive sources may be minimized in some applications to improve system sensitivity and to reduce measurement time. Furthermore, when high resolutions are desired, the mask projection tends to be magnified and lowering the distance between the source and camera system is also necessary (assuming that the distance between the mask and

the detector is fixed). However, when the distributed source image is produced by the cross-correlation method within near-field geometry, such as for scintimammography examinations, there are always obvious artifacts present [12]. In astronomy and nuclear medicine imaging, masks and anti-masks are used to reduce such artifacts [13–16]. By using maximum-likelihood expectation-maximization (MLEM) deconvolution methods, near-field artifacts and aperture collimation effects can also be reduced [17,18]. However, relatively few studies have been conducted on the use of the “blank-phantom”, which entails extracting the projected image of a uniformly distributed source from the phantom projection before using cross-correlations as an alternative decoding method [19].

To address the problems outlined above, we propose an experimental setup and a Geant4-based computational framework to model a specific scintimammography imaging setup. Moreover, the object-oriented (C++) toolkit for Monte Carlo simulation of particle transport through matter, Geant4 (GEometry ANd Tracking version 4), was used for different applications including high-energy physics, space dosimetry, medical imaging, medical dosimetry, radiation therapy and radiation protection [20–22]. Other than the possibility of tailoring realistic detector geometry, a range of functionalities is included in Geant4, such as tracking, geometry, physics models and hits. Additionally, the comprehensive range of physical processes, including electromagnetic, hadronic and optical processes, as well as long-lived particles, materials and elements over a wide energy range made it a versatile simulation opportunity. The framework consists of the full modeling of an anthropomorphic breast phantom, a NaI(Tl) crystal-based detector and a 41×41 MURA mask. Our three main goals can be summarized as follows: (1) experimental measurement of projected images, (2) verification of Geant4, and (3) computationally searching for tumor detection and localization. Thus, we first conducted an experimental procedure for imaging an in-house anthropomorphic breast phantom including a ^{99m}Tc source at different locations and an in-house designed and fabricated lead-based MURA mask (with 41×41 matrix). Second, we carried out some simulations for comparison purposes. Finally, we used the Geant4-based program to change the source location and to analyze the projected images. For all tests, we always used the “blank-phantom” method for image decoding and observe full width at half maximum (FWHM) and the contrast parameter. Researchers and technicians in radiation therapy, as well as students and technicians will find this study fascinating, as it continues radiation therapy research outside of imaging.

2. Materials and Methods

In the following subsections, we first describe the experimental setup used for point spread function (PSF) calculation and for a small tumor located within an anthropomorphic phantom imaging. Then, the Monte Carlo simulation procedure carried out to benchmark experimental data and to extend our work to other imaging scenarios is provided. Finally, as the coded-aperture (MURA mask) imaging needed a decoding stage, we briefly give the followed decoding code.

2.1. Experimental Setup

Figure 1 shows the experimental setup used including the anthropomorphic breast tissue phantom, the MURA mask, the mask holder and the imaging detector. Measurements have been performed with a Gamma-Camera Philips Brightview at King Khaled University Hospital (KKUH) and a 512×512 detector Field of View (FOV). The image acquisition time was set to 20 min, and the ^{99m}Tc source activity was 30 mCi. For each point of measurement, we repeated the experiment three times.

2.2. Simulation Procedure

In this work, we used a breast phantom, a MURA mask and a special detector. The breast phantom was modeled with the material composition taken from the NIST website (G4_ADIPOSE_TISSUE_ICRP) [23], and the geometry consists of the superposition of both a cylinder (50 cm radius and 35 cm height) and a semi-ellipsoid ($5 \times 5 \times 7 \text{ cm}^3$).

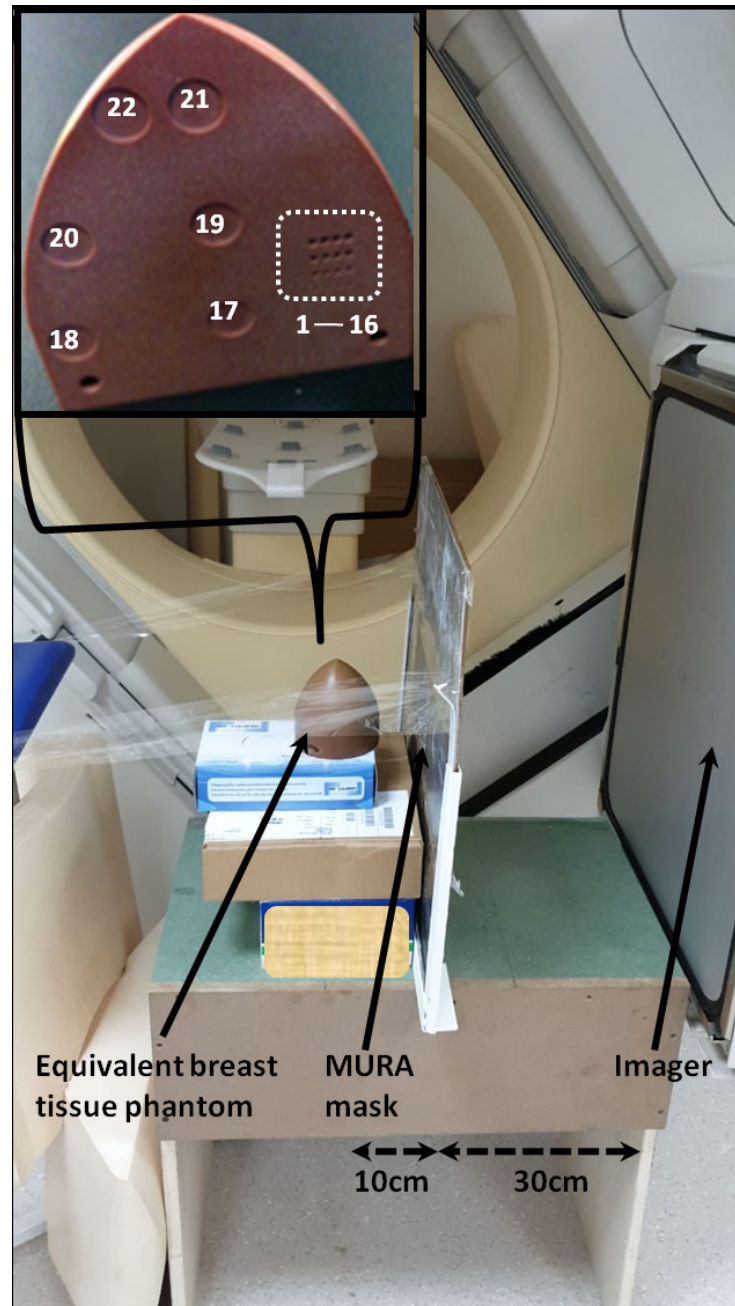


Figure 1. Experimental setup including equivalent tissue anthropomorphic breast phantom, MURA mask and imager. Twenty-two possible locations for the inserted ^{99m}Tc were also given.

Additionally, as seen in Figure 1, the phantom includes 22 possible locations (with the same thicknesses of 0.1 cm) for tumor positioning. Locations from 17 to 22 have the same radius of 1.2 cm; however, the other 16 options have different radii from 0.1 to 0.25 cm. All locations were cylindrical and filled with air as the medium. On the other hand, the MURA mask consists of a 41×41 array pattern. Designed at the center of a thin sheet holder of lead with the dimension of $60 \times 60 \times 0.15 \text{ cm}^3$, the mask was formed with a given distribution of box-shaped holes ($0.2 \times 0.2 \times 0.15 \text{ cm}^3$), resulting in a global dedicated volume of $8.2 \times 8.2 \times 0.15 \text{ cm}^3$. Similar to the desired mask, as described in the literature, it contains 50% open/close area, i.e., the same surface area of gamma ray-opaque and gamma-ray-transparent zones. A more detailed description was given by Kadri et al. [11]. Moreover, the detection system consists of the NaI(Tl) crystal detector with a surface of $0.597 \times 0.597 \text{ cm}^2$ and a thickness of 0.95 cm. The detector was pixelated onto 512×512 scoring pixels.

On the other hand, the generated energy spectrum follows a Gaussian distribution with 140.5 keV and 11.85 keV as the mean value and standard deviation, describing the ^{99m}Tc emission spectrum. With each simulation, we activated the Bremsstrahlung, ionization and multiple scattering models for electrons with an energy threshold of 990 eV. This allowed particles to be tracked almost entirely. A cutoff energy of 990 eV was used to activate the Compton effect, the photoelectric effect, and the Rayleigh scattering of the photon particles. A specific physics builder called 'G4EmStandardPhysics' was used to implement our electromagnetic physics options. As a result of Geant4's multithreading feature [24,25], all of the simulations ran in a reasonable amount of time, despite the complex experimental setup.

This near-field and medium phantom size application required a magnification factor of 3.0, so we fixed the mask-to-detector distance to be three times the source-to-mask distance. In order to create coded images, the detector crystal was illuminated with particles that deposited energy in it. All simulations were conducted on laptops (for testing) and Dell Precision T7610 workstations, each with a 40-core Intel Xeon E5-2680v2 CPU running at 2.80 GHz and 256 GB RAM. Ubuntu 14.04 was used to manage the entire workflow. Since we focused the generation toward the MURA mask, we generated more than 2×10^9 primary particles. Due to the open area (holes) constituting 50% the field of view, the number of counts detected (primary particles) through the MURA mask was half that of the generated primaries. The run time ranged from 20 min to more than 7 h, resulting in 1% statistical uncertainty for all studied cases.

2.3. Decoding Program

Basically, the coded aperture imaging procedure involved the construction of the decoding matrix (G_{ij}) corresponding to the mask-array pattern (A_{ij}) in order to reconstruct an image from its projection, in the following way [26]:

$$G_{ij} = \begin{cases} 1 & \text{if } i + j = 0 \\ 1 & \text{if } A_{ij} = 1, (i + j) \neq 0 \\ -1 & \text{if } A_{ij} = 0, (i + j) \neq 0 \end{cases} \quad (1)$$

For this purpose, we developed a matlab-based program for decoding and analyzing data.

3. Results and Discussion

In the following subsections, we present and discuss the verification procedure against the experimental tests carried out for the simulation using the Geant4 toolkit for PSF and other specific tumor-like locations within an anthropomorphic breast phantom. Moreover, the virtual generalization of TBR and the tumor location study for other situations is conducted using Geant4 toolkit.

3.1. Geant4 Benchmark

The Geant4 setup including the breast model (red), the MURA mask (blue) and the imaging detector is shown in Figure 2.

However, five experimental and simulated imaging scenarios are shown in Figures 3 and 4. We see the point spread function and tumor located at positions 8, 17, 19 and 21 of the anthropomorphic breast projections and corresponding decoded images, denoted as (a), (b), (c), (d) and (e), respectively.

The comparison of the measured and the calculated normalized PSF in terms of profile distributions allowed us to conclude their similarities. Moreover, the average and the standard deviation values were found to be 0.39 ± 0.37 and 0.41 ± 0.38 for the experimental and the simulation procedures, respectively, showing an error of 6% that can be explained by systematic and experimental related errors. First, a good agreement between the simulations and measurements is achieved.

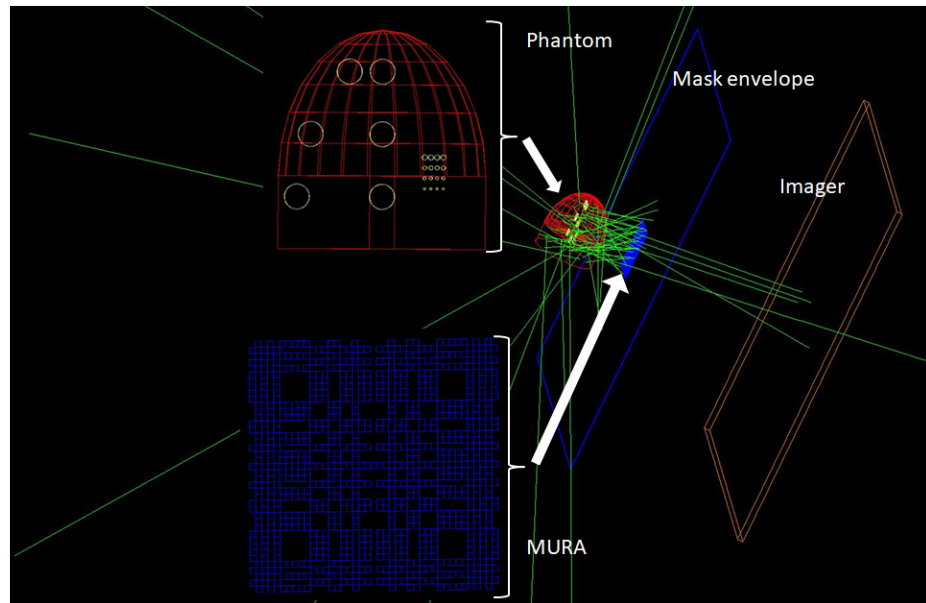


Figure 2. Geant4 setup visualization including the breast model (red), the MURA mask (blue), the imaging detector (orange) and the scattered photons trajectories (green lines). Zoomed out phantom and mask were also shown.

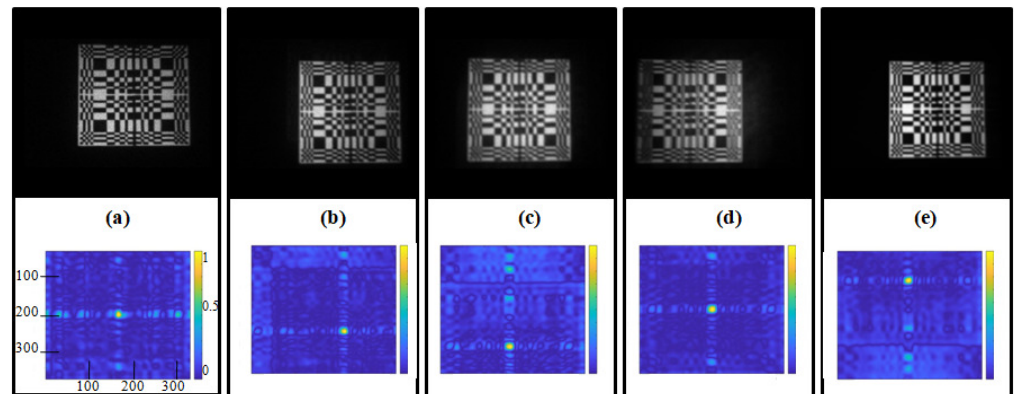


Figure 3. Five measured (up) images and decoded (down) experimental images: (a) PSF, (b) location 8, (c) location 17, (d) location 19 and (e) location 21. The same scale and legend remains valid for other subplots, as given in (a).

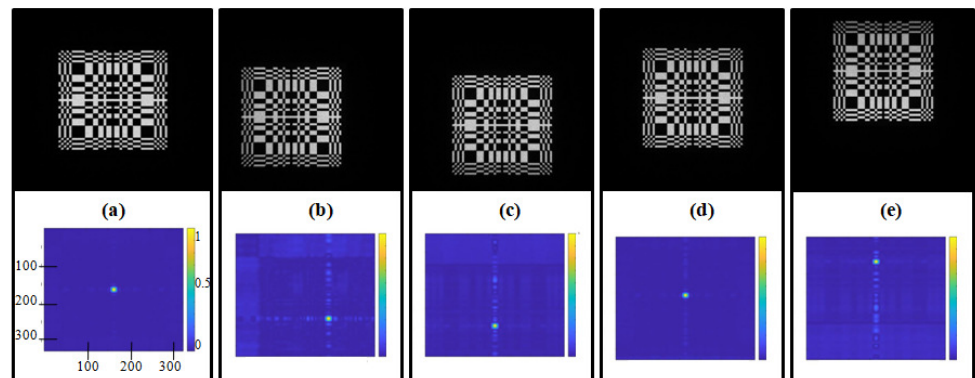


Figure 4. Five Geant4 simulated (up) and decoded (down) images: (a) PSF, (b) location 8, (c) location 17, (d) location 19 and (e) location 21. The same scale and legend remains valid for other subplots, as given in (a).

Thus, the developed Geant4-based program can correctly predict MURA mask scintimammography. Second, The spot position, shown in the decoded image, is directly related to the tumor position within the phantom. Hence, as location 19 is located near the central axis of the mask and below location 21 and over location 17, as seen in Figure 1, subfigures (a), (c), (d) and (e) confirm such a positioning in the decoded images. Additionally, location 8, situated on the right side of location 19, obeys the same conclusions. Finally, we can safely expand our work by simulating other scenarios.

3.2. Simulation Extended Work

As seen from Figures 5 and 6, we can calculate the full width at half maximum and the signal-to-background ratio (here denoted by a contrast parameter) for a given imaging configuration. Moreover, the simulation of different TBR values and locations allowed us to tabulate the data in Table 1. A comparison of the simulated data corresponding to locations 17–22 (almost completely occupying the whole phantom volume) led to an FWHM varying from 7.91 to 8.08 mm and a contrast varying from 3.29 to 4.07. Similarly, FWHM and contrast values vary from 7.84 to 8.09 and from 3.27 to 4.21, respectively, for locations 1–16. We can conclude that all of the configurations were detectable with an average FWHM of 7.99 ± 0.04 mm and contrast parameter of 3.71 ± 0.18 mm.

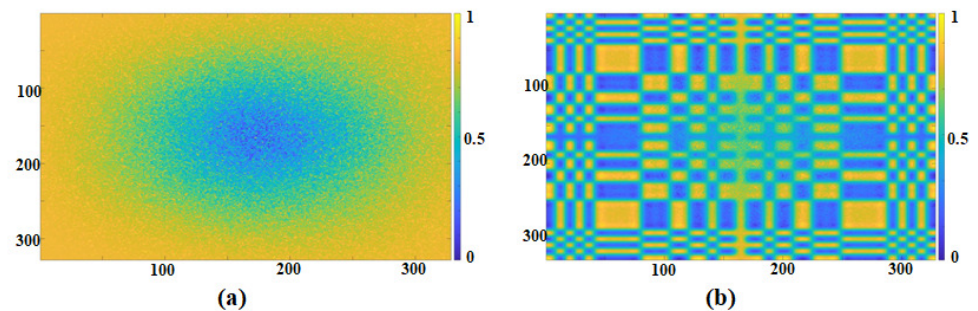


Figure 5. Simulated (a) and decoded (b) image for location 17 and TBR = 10.

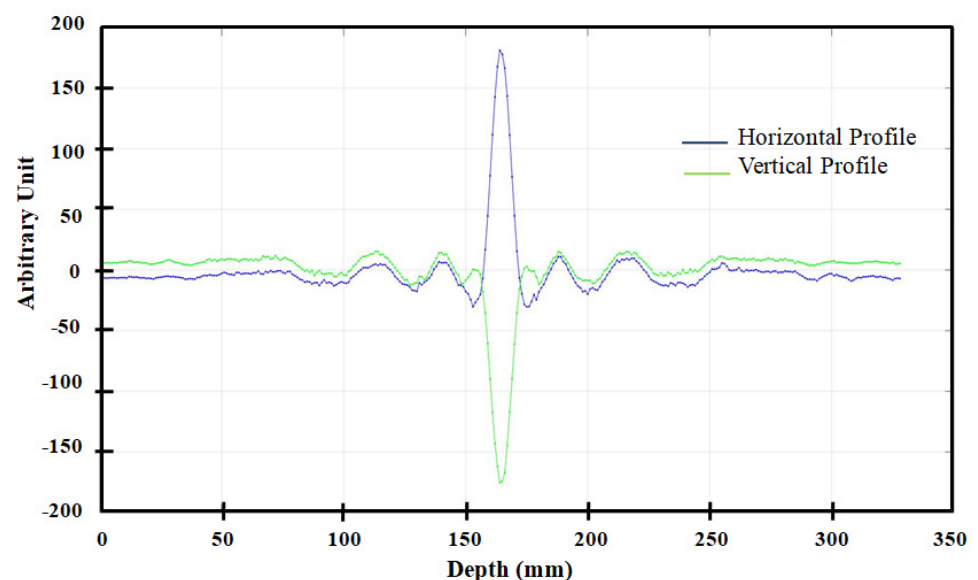


Figure 6. Horizontal and vertical profiles for decoded image of the studied case: location 17 and TBR = 10.

Table 1. FWHM and contrast parameter for all 22 studied locations and 9 TBR possibilities.

Location	TBR	FWHM	Contrast	Location	TBR	FWHM	Contrast
1	2	8.002	3.782	6	2	7.838	3.830
	3	7.985	3.968		3	7.962	3.693
	4	8.004	3.455		4	8.048	4.047
	5	7.932	3.686		5	7.990	3.686
	6	8.004	3.664		6	8.052	3.603
	7	8.049	3.978		7	7.910	3.591
	8	7.990	3.914		8	7.952	3.707
	9	7.885	3.914		9	8.052	3.719
	10	8.055	3.855		10	8.029	3.587
	2	2	8.030		3.718	7	2
3		7.998	3.268	3	7.929		3.880
4		7.931	3.608	4	7.962		3.857
5		8.042	3.616	5	7.928		3.518
6		7.909	3.856	6	7.943		4.021
7		8.053	4.059	7	7.981		4.048
8		8.049	3.736	8	8.002		3.499
9		7.975	3.320	9	8.025		3.660
10		7.971	3.524	10	7.933		3.799
3		2	7.973	3.413	8		2
	3	8.021	3.739	3		8.033	3.699
	4	7.986	3.467	4		7.948	3.603
	5	7.982	3.788	5		7.925	3.772
	6	8.002	3.819	6		8.017	3.572
	7	7.927	3.615	7		8.007	3.664
	8	8.018	3.959	8		7.975	3.872
	9	8.069	3.678	9		7.975	3.822
	10	7.977	3.418	10		7.988	3.469
	4	2	8.065	3.809		9	2
3		7.936	3.623	3	7.954		3.665
4		7.993	3.871	4	7.957		3.629
5		8.018	3.398	5	7.915		3.751
6		8.009	3.844	6	7.962		3.741
7		7.940	3.990	7	8.013		3.690
8		8.010	3.601	8	8.033		3.887
9		8.005	3.784	9	7.913		3.498
10		7.999	3.871	10	7.957		3.300

Table 1. Cont.

Location	TBR	FWHM	Contrast	Location	TBR	FWHM	Contrast
5	2	7.984	3.696	10	2	8.085	3.845
	3	7.897	3.871		3	7.961	3.666
	4	8.004	3.465		4	7.936	3.875
	5	7.973	3.842		5	8.088	4.207
	6	7.939	3.700		6	8.040	3.724
	7	7.918	3.740		7	8.016	3.723
	8	7.975	3.914		8	7.895	3.563
	9	8.009	3.685		9	8.050	3.669
	10	7.949	3.721		10	8.030	3.830
	11	2	8.042		3.898	17	2
3		7.978	3.701	3	7.933		3.426
4		8.025	3.811	4	7.973		3.728
5		7.838	3.352	5	7.994		3.691
6		7.964	3.831	6	7.999		3.731
7		7.999	4.126	7	7.931		3.892
8		7.958	3.399	8	7.981		3.505
9		8.035	3.776	9	7.927		3.852
10		7.956	3.635	10	8.050		3.821
12		2	7.955	3.651	18		2
	3	8.010	3.537	3		7.930	3.570
	4	7.882	3.889	4		7.984	3.372
	5	7.982	3.638	5		7.961	3.897
	6	7.970	3.960	6		8.046	3.640
	7	7.984	3.888	7		7.911	3.520
	8	8.004	3.616	8		7.987	3.530
	9	7.921	3.718	9		8.078	3.667
	10	7.986	4.050	10		8.001	3.992
	13	2	7.995	3.593		19	2
3		7.966	4.072	3	7.981		3.843
4		7.984	3.590	4	7.975		3.780
5		7.977	3.505	5	7.994		3.711
6		8.006	3.748	6	8.002		3.846
7		7.988	3.812	7	7.936		3.880
8		7.973	3.770	8	7.956		3.355
9		8.081	3.859	9	7.978		3.704
10		7.944	4.022	10	8.007		3.294

Table 1. Cont.

Location	TBR	FWHM	Contrast	Location	TBR	FWHM	Contrast
14	2	8.037	3.510	20	2	7.949	3.830
	3	8.000	3.707		3	7.987	3.655
	4	8.023	3.612		4	8.030	3.492
	5	7.925	3.930		5	7.966	3.903
	6	8.015	3.519		6	7.951	3.582
	7	7.979	3.843		7	7.967	3.782
	8	8.015	3.523		8	8.017	3.814
	9	8.033	3.440		9	8.008	3.642
	10	7.936	3.542		10	8.018	3.451
	15	2	7.982		3.623	21	2
3		8.007	3.745	3	8.002		3.364
4		7.959	3.696	4	7.982		3.512
5		7.975	3.742	5	8.003		4.029
6		8.005	4.063	6	8.074		3.803
7		7.974	3.718	7	7.996		3.598
8		7.957	3.642	8	8.021		3.795
9		7.935	3.886	9	7.982		3.828
10		7.955	3.499	10	8.050		3.636
16		2	8.035	3.641	22		2
	3	7.985	3.487	3		8.011	3.586
	4	7.968	3.722	4		8.050	3.678
	5	8.069	3.465	5		7.975	3.988
	6	8.084	3.713	6		7.937	3.867
	7	7.999	3.587	7		7.944	3.551
	8	7.935	3.718	8		8.019	4.012
	9	8.054	3.496	9		7.996	3.767
	10	8.019	3.637	10		7.926	3.874

Hence, a summary of the average and the standard deviation of FWHM and contrast parameter for all studied locations (data in Table 2) were given for more clarification.

Previous remarks confirm that other work [11,19] declared the possible use of MURA mask as an alternative to collimators for scintimammography imaging modalities. However, our next work will be conducted to experimentally verify those parameters for lower tumor sizes. Nevertheless, the current study can be of interest to physicians and to medical staff communities as an advancement on the topic of using MURA masks for scintimammography.

Table 2. A summary of the average and the standard deviation of FWHM and contrast parameter for all studied locations.

Location	FWHM		Contrast	
	Average	Stdev	Average	Stdev
1	7.989	0.053	3.802	0.173
2	7.989	0.051	3.600	0.256
3	8.005	0.045	3.699	0.175
4	7.988	0.030	3.742	0.181
5	7.958	0.040	3.742	0.141
6	7.982	0.074	3.718	0.145
7	7.966	0.036	3.790	0.197
8	7.979	0.035	3.716	0.159
9	7.976	0.056	3.667	0.180
10	8.002	0.065	3.782	0.197
11	7.968	0.057	3.698	0.233
12	7.970	0.042	3.765	0.184
13	7.995	0.041	3.765	0.205
14	7.990	0.038	3.637	0.162
15	7.978	0.032	3.737	0.160
16	8.014	0.052	3.603	0.110
17	7.979	0.043	3.747	0.197
18	7.981	0.055	3.650	0.192
19	7.975	0.024	3.694	0.218
20	7.995	0.028	3.647	0.158
21	8.011	0.032	3.692	0.196
22	7.982	0.044	3.790	0.175

4. Conclusions

The application of Monte Carlo simulation techniques to breast imaging is necessary today in terms of predicting and assessing existing scenarios. Since small-sized tumors are still an open topic, this study is an extension of previous work [11], in which MURA masks were used for breast imaging to overcome the difficulty of detecting these tumors. An anthropomorphic prone breast was modeled using Geant4-based simulations including small tumors spread over three locations (skin layer, central axis, and between them) and with tumor-to-background ratios ranging from 2 to 10. We verified that the simulations predicted the experimentally measured images given the setups for which they were performed. Furthermore, the benefits of using MURA-mask images combined with a phantom blank subtraction decoding method ($TBR = 1$) have been established. Additionally, we calculated the full width at half maximum and contrast for decoded images, and this helped us to better localize tumors of small sizes with lower uptake. Further investigation into this topic by studying image processing techniques in depth will be beneficial in the future. Even so, this study would be a good step forward for a large multidisciplinary community of physicians, medical professionals, and students interested in exploring and learning about early tumor detection by scintimammography.

Author Contributions: Conceptualization, methodology, investigation, experimentation, writing—original draft preparation, writing—review and editing, M.A.A., K.S. and O.K. All authors have read and agreed to the published version of the manuscript.

Funding: This research received no external funding.

Institutional Review Board Statement: Not applicable.

Informed Consent Statement: Not applicable.

Data Availability Statement: Not applicable.

Acknowledgments: This work was supported by The National Plan for Science, Technology and Innovation (MAARIFAH), King Abdulaziz City for Science and Technology, Kingdom of Saudi Arabia, Award Number (12-MED2516-02).

Conflicts of Interest: The authors declare no conflict of interest.

Abbreviations

The following abbreviations are used in this manuscript:

MURA	Modified Uniformly Redundant Array
FWHM	Full Width at Half Maximum
PSF	Point Spread Function
FOV	Field Of View
TBR	Tumor-to-Background Ratio

References

- Mladenov, A.; Stankov, D.; Nonova, T.; Krezhov, K. Radiation protection, radioactive waste management and site monitoring at the nuclear scientific experimental and educational centre IRT-Sofia at INRNE-BAS. *Radiat. Prot. Dosim.* **2014**, *162*, 176–181. [[CrossRef](#)] [[PubMed](#)]
- Ambrosino, F.; Thinova, L.; Briestensky, M.; Giudicepietro, F.; Roca, V.; Sabbarese, C. Analysis of geophysical and meteorological parameters influencing ²²²Rn activity concentration in Mladec caves (Czech Republic) and in soils of Phlegrean Fields caldera (Italy). *Appl. Radiat. Isot.* **2020**, *160*, 109140. [[CrossRef](#)] [[PubMed](#)]
- Zhang, K.; Zeng, Y.; Liu, Z.; Cao, H.; Zhu, W. Investigation on the radiation decontamination of lanthanum oxide during its production from ion-adsorption rare earth ores in China. *Hydrometallurgy* **2019**, *189*, 105117. [[CrossRef](#)]
- Das, B.K.; Biswal, B.M.; Bhavaraju, M. Role of scintimammography in the diagnosis of breast cancer. *Malays. J. Med. Sci.* **2006**, *13*, 52–57.
- Paradiso, V.; Crivellaro, A.; Amgarou, K.; de Lanaute, N.B.; Fua, P.; Lienard, E. A versatile calibration procedure for portable coded aperture gamma cameras and RGB-D sensors. *Nucl. Instrum. Methods Phys. Res. A* **2018**, *886*, 125–133. [[CrossRef](#)]
- Amgarou, K.; Paradiso, V.; Patoz, A.; Bonnet, F.; Handley, J.; Couturier, P.; Becker, F.; Menaa, N. A comprehensive experimental characterization of the iPIX gamma imager. *J. Instrum.* **2016**, *11*, 08012. [[CrossRef](#)]
- Sun, S.; Zhang, Z.; Shuai, L.; Li, D.; Wang, Y.; Liu, Y.; Huang, X.; Tang, H.; Li, T.; Chai, P. Development of a panorama coded-aperture gamma camera for radiation detection. *Radiat. Meas.* **2015**, *77*, 34–40. [[CrossRef](#)]
- Sun, S.; Zhang, Z.; Shuai, L.; Li, D.; Wang, Y.; Liu, Y.; Huang, X.; Tang, H.; Li, T.; Chai, P. Far field 3D localization of radioactive hot spots using a coded aperture camera. *Appl. Radiat. Isot.* **2016**, *107*, 177–182.
- Dubos, S.; Lemaire, H.; Schanne, S.; Limousin, O.; Carrel, F.; Schoepff, V.; Blondel, C. ORIGAMIX, a CdTe-based spectro-imager development for nuclear applications. *Nucl. Instrum. Methods Phys. Res. A* **2015**, *787*, 302–307. [[CrossRef](#)]
- Zhang, R.; Gong, P.; Tang, X.; Wang, P.; Zhou, C.; Zhu, X.; Gao, L.; Liang, D.; Wang, Z. Reconstruction method for gamma-ray coded-aperture imaging based on convolutional neural network. *Nucl. Instrum. Methods Phys. Res. A* **2019**, *934*, 41–51. [[CrossRef](#)]
- Kadri, O.; Alfuraih, A. Monte Carlo assessment of coded aperture tool for breast imaging: A Mura-mask case study. *Nucl. Sci. Tech.* **2019**, *30*, 164. [[CrossRef](#)]
- Zhang, T.; Wang, L.; Ning, J.; Lu, W.; Wang, X.F.; Zhang, H.W.; Tuo, X.G. Simulation of an imaging system for internal contamination of lungs using MPA-MURA coded aperture collimator. *arXiv* **2021**, arXiv:2101.07442.
- Penacchioni, A.V.; Braga, J.; Castro, M.A.; D’Amico, F. Telescope performance and image simulations of the balloon-borne coded-mask protoMIRAX experiment. *J. High Energy Astrophys.* **2015**, *5–6*, 22–29. [[CrossRef](#)]
- Accorsi, R.; Lanza, R.C. Near-field artifact reduction in planar coded aperture Imaging. *Appl. Opt.* **2001**, *40*, 4697–4705. [[CrossRef](#)]
- Braga, J.; Durao, O.S.C.; Castro, M.; D’Amico, F.; Stecchini, P.E.; Amirabile, S.; Blanco, F.G.; Strauss, C.; Silva, W.; Schad, V.R.; et al. LECX: A cubesat experiment to detect and localize cosmic explosions in hard X-rays. *Mon. Not. R. Astron. Soc.* **2020**, *493*, 4852–4860. [[CrossRef](#)]
- Kasuga, T.; Odaka, H.; Hatauchi, K.; Takashima, S.; Tamba, T.; Aizawa, Y.; Hashiba, S.; Bamba, A.; Zhou, Y.; Tamagawa, T. Artifact-less Coded Aperture Imaging in the X-ray Band with Multiple Different Random Patterns. *arXiv* **2020**, arXiv:2007.15278.
- Jeong, M.; Hammig, M.D. Comparison of gamma ray localization using system matrixes obtained by either MCNP simulations or ray-driven calculations for a coded-aperture imaging system. *Nucl. Instrum. Methods A* **2018**, *954*, 161353. [[CrossRef](#)]
- Sun, S.; Liu, Y.; Ouyang, X. Near-field high-resolution coded aperture gamma-ray imaging with separable masks. *Nucl. Instrum. Methods A* **2020**, *951*, 163001. [[CrossRef](#)]
- Alnafea, M.; Wells, K.; Spyrou, N.M.; Guy, M. Preliminary Monte Carlo study of coded aperture imaging with a CZT gamma camera system for scintimammography. *Nucl. Instrum. Methods A* **2007**, *573*, 122–125. [[CrossRef](#)]
- Agostinelli, S.; Allison, J.; Amako, K.A.; Apostolakis, J.; Araujo, H.; Arce, P.; Asai, M.; Axen, D.; Banerjee, S.; Barrand, G.J.N.I.; et al. GEANT4—a simulation toolkit. *Nucl. Instrum. Methods A* **2003**, *506*, 250–303. [[CrossRef](#)]
- Beaudoux, V.; Blina, G.; Barbrelb, B.; Kantorc, G.; Zacharatou, C. Geant4 physics list comparison for the simulation of phase-contrast mammography (XPulse project). *Phys. Medica* **2019**, *60*, 66–75. [[CrossRef](#)] [[PubMed](#)]

22. Rinaldi, L.; Ambrosino, F.; Roca, V.; D'Onofrio, A.; Sabbarese, C. Study of $^{222-220}\text{Rn}$ Measurement Systems Based on Electrostatic Collection by Using Geant4+COMSOL Simulation. *Appl. Sci.* **2022**, *12*, 507. [[CrossRef](#)]
23. Berger, M.J.; Coursey, J.S.; Zucker, M.A.; Chang, J. *Stopping-Power & Range Tables for Electrons, Protons and Helium Ions*; NIST Standard Reference Database 124 2017, NISTIR 4999; National Institute of Standards and Technology: Gaithersburg, MD, USA, 2017.
24. Allison, J.; Amako, K.; Apostolakis, J.; Arce, P.; Asai, M.; Aso, T.; Bagli, E.; Bagulya, A.; Banerjee, S.; Barrand, G.J.N.I.; et al. Recent developments in GEANT4. *Nucl. Instrum. Methods A* **2016**, *835*, 186–225. [[CrossRef](#)]
25. Cosmo, G.; The Geant4 Collaboration. Geant4-towards major release 10. *J. Phys. Conf. Ser.* **2014**, *513*, 022005. [[CrossRef](#)]
26. Cieslak, M.J.; Gamage, K.A.; Glover, R. Coded-aperture imaging systems: past, present and future development—A review. *Radiat. Meas.* **2016**, *92*, 59–71. [[CrossRef](#)]